New Astronomy 108 (2024) 102174

Contents lists available at ScienceDirect

New Astronomy

journal homepage: www.elsevier.com/locate/newast

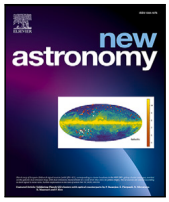

Evidence of a sub-solar star in a microlensing event toward the LMC

A. Franco *, A.A. Nucita, F. De Paolis, F. Strafella

Department of Mathematics and Physics "E. De Giorgi" , University of Salento, Via per Arnesano, CP-I93, I-73100, Lecce, Italy
INFN, Sezione di Lecce, Via per Arnesano, CP-193, I-73100, Lecce, Italy
INAF, Sezione di Lecce, Via per Arnesano, CP-193, I-73100, Lecce, Italy

ARTICLE INFO

Keywords:
Physical data and processes
Gravitational lensing
Methods
Data analysis
Techniques
Image processing
(Galaxies) Large Magellanic Clouds

ABSTRACT

Gravitational microlensing is known to be an impressive tool for searching dark, small, and compact objects that are missed by the usual astronomical observations. In this paper, by analysing multiple images acquired by DECam, we present the detection and a complete description of the microlensing event LMC J05074558-65574990 which is most likely due to a sub-solar object with mass $(0.16 \pm 0.10)\ M_{\odot}$, hence in the mass range between a massive brown dwarf and a red dwarf, whose distance is estimated to be $7.8^{+4.1}_{-3.4} \times 10^2$ pc thanks to the Gaia observation of the source, leading us to consider this lens as one the closest ever detected.

1. Introduction

Since the discovery of the first microlensing event in 1989 (Irwin et al., 1989) and the results obtained by some important observational campaigns like OGLE (Udalski et al., 1993), MACHO (Alcock et al., 1996) and EROS (Palanque-Delabrouille et al., 1998), the search for microlensing candidates became more resolute. In particular, dense and crowded regions, such as those toward the Galactic Bulge and the Magellanic Clouds, have always been preferred in order to test new galactic models, searching for any evidence of dark objects acting as gravitational lenses.

For events induced by a single lens, the typical brightness profile, the so called Paczyński function (Paczyński, 1986), shows a flux variation delineated by a symmetric and achromatic light curve. However, sometimes the light curve may be distorted or broadened due to secondary effects, such as the Earth parallax (due to annual Earth motion around the Sun) and the finite source (due to the not negligible finite angular size of the source that cannot be approximated to a single point) as described in Gould (1992) and Gould and Salim (2000).

By fitting a simple Point-Lens Point-Source event, one cannot entirely resolve the system, since there is no way to obtain a direct estimate of both the lens distance and mass. However a Monte Carlo simulation can give useful statistical indication of the system parameters (see Ingrosso et al. 2006).

In the present paper we report about the discovery of a microlensing event labelled as LMC J05074558-65574990 ($\alpha = 05^h07^m45.58^s$, $\delta = -65°57'49.90\varepsilon$; $l = 276°.662903$, $b = -36°.218246$) as a possible sub-solar object candidate, particularly close to Earth. We show the result obtained by analysing repeated images acquired by DECam in three SDSS bands (*g*, *r*, and *i*) confirming the achromaticity feature of the detected microlensing event, following the same data reduction and photometric procedure adopted in Franco et al. (2023b).

The paper is structured as follows: in Section 2, we give some details about the observational survey considered in this work, some information about the target source and a description of the analysis conducted in order to obtain the calibrated light curves. We also describe the usage of the *pyLIMA* software (Bachelet et al., 2017) for the modelling of the microlensing event. In Section 3, we give details on the different microlensing models taken into account specifying the best one we chose, i.e. the simpler Point-Source Point-Lens model, addressing then our conclusion in Section 4.

2. Observations and data reduction

The discovered microlensing event has been detected by analysing multiple temporally sorted images acquired by DECam (Dark Energy Camera)[1] during the two-year CTIO program (2018A-0273),[2] intensively observing the Magellanic Clouds between February 2018 and January 2020 (see Franco et al. 2023a,b for more details). In particular, we used observations obtained in three different DECam bands, i.e. *g*, *r*,

* Corresponding author at: Department of Mathematics and Physics "E. De Giorgi" , University of Salento, Via per Arnesano, CP-I93, I-73100, Lecce, Italy.
E-mail address: antonio.franco@le.infn.it (A. Franco).

[1] The Dark Energy Camera is a high-performance, wide-field camera installed at the 4 m V. Blanco Telescope, CTIO, Chile (Flaugher et al., 2015).

[2] The proposed survey project with the title "PALS: Paralensing Survey of Intermediate Mass Black Holes" was originally planned to potentially identify microlensing events induced by Intermediate-Mass Black Holes.

https://doi.org/10.1016/j.newast.2023.102174
Received 17 June 2023; Received in revised form 9 November 2023; Accepted 4 December 2023
Available online 5 December 2023

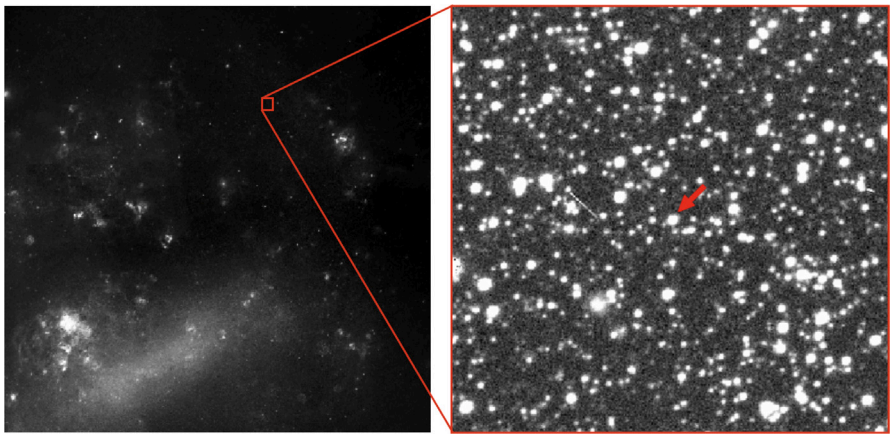

Fig. 1. Large portion of the LMC (left panel) in which the interested DECam field is observed (right panel). The red arrow in the right panel indicates the microlensing candidate position as observed by DECam.

and *i*, that correspond to the respective SDSS bands. Specifically, the observed source has been captured in 37 *g* band, 49 *r* band, and 7 *i* band images. We also checked *ESA XMM-Newton* and *NASA Swift* images for any X-ray counterpart of the target source, considering its potential as a cataclysmic variable. However, we did not find any correlation, reinforcing the conclusion that the most plausible explanation remains the microlensing scenario.

In Fig. 1 we present an image of the LMC field, obtained by DECam, in which the lensed source star is located. The star is also present in GaiaDR3 (Gaia Collaboration et al., 2022), where it is catalogued as a star located in the Galactic thick-disk at a distance of $1.55^{+0.72}_{-0.53}$ kpc from Earth (Bailer-Jones et al., 2021) that derives from the assumption that the object is single (as explicitly remarked by Bailer-Jones et al. 2021).[3] The Gaia magnitudes reported in the catalogue are 20.33, 20.88, and 19.77 in the G, BP, and RP bands, respectively.

The source surface temperature can be estimated by considering the B-V colour index. The observed values can be extracted from the catalogue "Magellanic Clouds Photometric Survey: the LMC" (Zaritsky et al., 2004), which returns $B - V = 0.936 \pm 0.130$. By querying the ADS/IRSA database[4] at the object coordinates, the respective colour excess provided by Schlafly and Finkbeiner (2011) is $E(B - V) = 0.0812 \pm 0.0049$, and the true colour index becomes $B-V = 0.855 \pm 0.130$. Considering the well known colour index relation with the associated temperature, given by Ballesteros' formula (Ballesteros, 2012), the obtained surface temperature of the lensed star turns out to be $T_S = (5120 \pm 370)$ K, corresponding to a K1V spectral type star (Lang, 1992).

With the aim of obtaining the light curve of the source star, the acquired DECam observations, already corrected by bias, flat, and dark, have been aligned and processed by using the ISIS 2.2 subtraction package (Alard and Lupton, 1998; Alard, 2000), a powerful software capable of highlighting variable sources in a set of multiple temporally sorted images, employing a photometric analysis based on the difference between homogeneous images. The software returns a list of differential fluxes, evaluated as

$$\Delta f_{\rm i} = f_{\rm ref} - f_{\rm i} \tag{1}$$

where $f_{\rm ref}$ is the flux related to a reference image, chosen as that being characterised by the best signal-to-noise ratio, and f_i represents the flux corresponding to the *i*th image of the sample. Therefore, by evaluating a source flux ($f_{\rm ref}$) in the reference image with the DAOPHOT/ALLSTAR softwares (Stetson, 1996), the flux of the same source in the *i*th image is simply obtained by inverting the previous equation, thus giving

$$f_{\rm i} = f_{\rm ref} - \Delta f_{\rm i} \tag{2}$$

By adopting the procedure described in Franco et al. (2023b), we calibrated photometrically all the images with the ATLAS All-Sky Stellar Reference Catalogue (Tonry et al., 2018) and obtained the calibrated DECam magnitudes in the *g*, *r*, and *i* bands as

$$\begin{aligned} g &= 0.928 \cdot g_{\rm instr} + 6.463 \\ r &= 0.932 \cdot r_{\rm instr} + 6.082 \\ i &= 1.105 \cdot i_{\rm instr} + 4.902 \end{aligned} \tag{3}$$

where $g_{\rm instr}$, $r_{\rm instr}$, and $i_{\rm instr}$ are the corresponding instrumental magnitudes.

Once the photometric procedure was applied, the analysis of the microlensing candidate has been carried out with *pyLIMA*, a Python open-source package for microlensing modelling (Bachelet et al., 2017). We considered both a Point-Lens Point-Source (PSPL) model and a Finite-Source Point-Lens (FSPL) model, accounting also for the annual Earth parallax effect, as described in Gould (1992) and Alcock et al. (1995).

Based on this model, the fit considers up to twelve parameters, depending on the microlensing model considered: the time t_0 of minimum approach between the source and the lens, the minimum impact parameter u_0, the Einstein time $t_{\rm E}$, the source finite angular radius ρ in units of Einstein angle, the North and East parallax components $\pi_{\rm EN}$ and $\pi_{\rm EE}$, the baseline fluxes in the three bands (from which one can estimate the baseline magnitudes $m_{0,\rm g}$, $m_{0,\rm r}$ and $m_{0,\rm i}$) as well as the blending factors $g_{\rm g}$, $g_{\rm r}$ and $g_{\rm i}$ (see Section 3 for details).

3. Microlensing model

Gravitational lensing, i.e. one of the natural consequences of Einstein's General Relativity, shows up thanks to the gravitational effect of a massive object, the lens, which bends the light rays from a distant source, generating multiple virtual images, whose deflection angle (see Fig. 3) is $\alpha \approx \frac{4GM_L}{\theta D_L c^2}$ (Einstein, 1936), where M_L is the lensing object mass and D_L is its distance from Earth.

In a microlensing event, the angular separation of the produced images cannot be spatially resolved by a telescope. However, a light magnification $A(t)$ of the source brightness (Paczyński, 1986, 1996) given by

$$A(t) = \frac{u(t)^2 + 2}{u\sqrt{u(t)^2 + 4}} \tag{4}$$

[3] We note that the source distance is not the typical one expected for the sources in a microlensing campaign toward the LMC.

[4] Data Tag: ADS/IRSA.Dust#2023/0719/032229_22258.

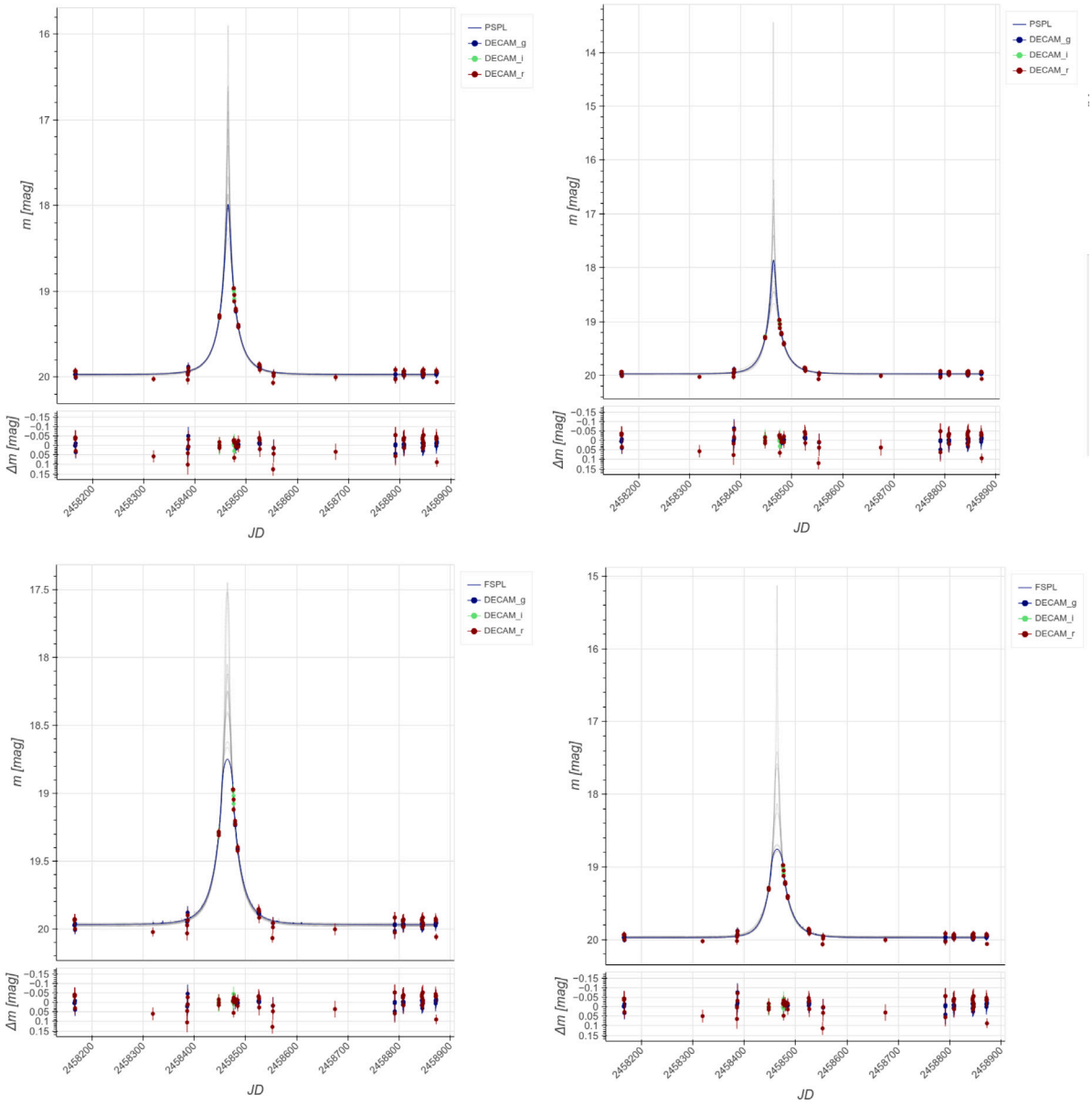

Fig. 2. In the four panels, the g-band (blue dots), r-band (red dots), and i-band (green dots) DECam data for the microlensing candidate are reported. The blue curve represents the best fit curve corresponding to the best-fit model adopted. In particular, the considered model corresponds to a Point-Source Point-Lens model (upper left), Point-Source Point-Lens model + Earth Parallax effect (upper right), Finite-Source Point-Lens (lower left) and Finite-Source Point-Lens + Earth Parallax (lower right). For each panel, the subpanel in the bottom shows the residuals for each band.

Table 1
Best fit results for the parameters of the four models considered for the LMC J05074558-65574990 microlensing event light curve. Asterisks (*) indicate the parameters not requested in the considered model.

	PSPL	PSPL + Parallax	FSPL	FSPL + Parallax
t_0 [MJD]	58464.6 ± 0.13	58355.4 ± 72.5	58464.6 ± 0.20	58323.18 ± 52.8
u_0	0.10 ± 0.07	0.85 ± 1.23	0.32 ± 0.09	0.52 ± 1.52
t_E [days]	40.2 ± 3.0	38.7 ± 1.5	38.2 ± 2.8	33.8 ± 1.2
ρ	*	*	0.44 ± 0.16	0.52 ± 0.17
π_{EN}	*	−0.15 ± 0.20	*	−0.28 ± 0.22
π_{EE}	*	0.56 ± 0.30	*	0.60 ± 0.25
$m_{0,g}$	20.55 ± 0.16	20.48 ± 0.10	20.37 ± 0.13	20.25 ± 0.10
g_g	0.71 ± 0.22	0.61 ± 0.14	0.45 ± 0.20	0.18 ± 0.09
$m_{0,i}$	20.15 ± 0.23	20.08 ± 0.10	19.96 ± 0.13	19.879 ± 0.09
g_i	0.03 ± 0.31	−0.19 ± 0.23	−0.04 ± 0.28	−0.31 ± 0.19
$m_{0,r}$	20.05 ± 0.20	19.92 ± 0.12	19.92 ± 0.17	19.68 ± 0.14
g_r	0.02 ± 0.13	−0.04 ± 0.08	−0.12 ± 0.14	−0.30 ± 0.05
χ^2 [NO-SCALING]	192	186	180	175
χ^2/dof [NO-SCALING]	2.29	2.27	2.17	2.15
χ^2	85	83	83	78
χ^2/dof	1.0	1.0	1.0	0.96

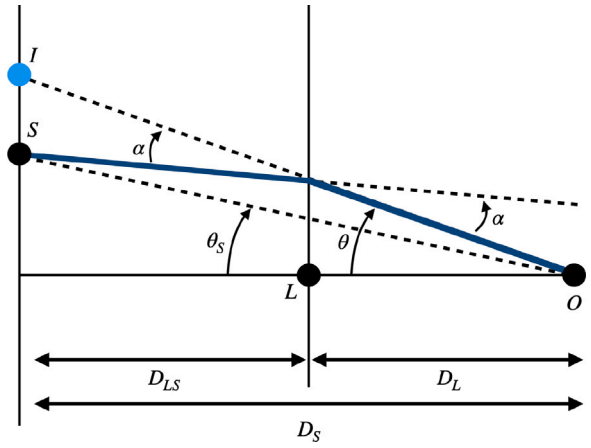

Fig. 3. Gravitational lensing geometry (see, e.g., De Paolis et al. 2016). The black dots represent the source (S), lens (L), and observer (O), respectively. The blue dot, labelled as I, indicates the position of the virtual image produced by the light deflection. The blue line indicates the path followed by light. Note that $D_{\rm L}$, $D_{\rm S}$, and $D_{\rm LS}$ are the distances to the lens, to the source star, and the lens-source distance, respectively. The angle α indicates the deflection angle, θ_S is the lens-source angular distance and θ is the lens-image angular distance.

can be observable. Here, $u(t) = \theta_S(t)/\theta_{\rm E}$ is the source-lens angular separation in Einstein angle unit (Fig. 3). It can be also expressed in terms of the event time-scale, named Einstein time $t_{\rm E}$

$$u(t) = \sqrt{u_0^2 + \left(\frac{t - t_0}{t_{\rm E}}\right)^2} \tag{5}$$

where, u_0 and t_0 are the impact parameter and the time, respectively, both considered at the minimum lens-photon approach.

The Einstein time depends on the transverse lens velocity relative to the observer-source line of sight v_t, and the Einstein radius $R_{\rm E}$ as

$$t_{\rm E} = \frac{R_{\rm E}}{v_t} = \frac{\theta_{\rm E} D_{\rm L}}{v_{\rm t}} \tag{6}$$

where $\theta_E = \sqrt{\frac{4GM_L}{c^2}\frac{D_S - D_L}{D_S D_L}}$ is the Einstein angle.

The amplified magnitude of the lensed stars can be computed through the usual relation

$$m(t) = m_0 - 2.5\log_{10}[(A(t) - 1)g + 1] - 2.5\log_{10} g \tag{7}$$

where m_0 is the baseline magnitude and g is the blending parameter. The latter parameter accounts for any possible flux contribution of the lensing object and/or nearby stars and is defined as

$$g = \frac{f_{\rm b}}{f_{\rm s}} \tag{8}$$

where $f_{\rm s}$ is the source flux[5] and $f_{\rm b}$ is the blended flux.

In this work, we considered four different models in order to better explain the analysed data. In particular, we firstly fit our data with a simple Point-Lens Point-Source (PSPL) model, in order to obtain a preliminary set of reliable values and good boundaries for the involved parameters. Afterwards, we related more accurate models: in particular, considering the Earth Parallax and the finite source possibility, we extended the first model adopted by using the PSPL+Earth Parallax and the Finite-Source Point-Lens (FSPL) models. Lastly, the most complex model, namely FSPL+Earth Parallax, has been taken into account. In the scenario of an extended source, the total amplification is obtained by integrating the amplification in Eq. (4) over the source area S. Considering the source angular radius (θ_S) in units of Einstein's angle $\rho = \theta_S/\theta_E$, the total amplification is

$$A^*(u,\rho) = \frac{\int_S A(t)\, dS}{\int_S dS} = \frac{1}{\pi\rho^2}\int_S A(t)\, dS \tag{9}$$

where $A(t)$ is given by the Point-Source Point-Lens model in Eq. (4). In the hypothesis of finite source effect, since our data show a quite small magnitude magnification of $\simeq 1 \div 2$, we are not able to introduce the approximated formula for $A(t)$ as proposed by Gould (1994).[6] Accordingly, we took into account the full non-approximated expression, implemented in pyLIMA by following a robust algorithm proposed by Lee et al. (2009).

Moreover, since ρ is defined as the source size in units of the Einstein angle, estimating the ρ value makes easier estimating the Einstein angle through the relation

$$\theta_{\rm E} = \frac{R_S}{\rho D_S} \tag{10}$$

where R_S and D_S are the source radius and the Earth-source distance, respectively.

Another relevant information that one can extract from the fit procedure is that related to the parallax effect induced by the Earth's motion around the Sun. It allows to estimate the value of the Einstein radius projected onto the observer plane, i.e. the reduced Einstein radius $\tilde{r}_{\rm E}$ (Gould, 1992; Gould and Salim, 2000) given by

$$\tilde{r}_{\rm E} = \theta_{\rm E}\frac{D_{\rm L} D_{\rm S}}{D_{\rm LS}} \tag{11}$$

The parallax parameter is then related to the reduced Einstein radius and to the Earth-Sun distance through the relation

$$\pi_{\rm E} = \frac{1\ {\rm AU}}{\tilde{r}_{\rm E}} \tag{12}$$

where 1 AU= 1.496×10^8 km indicates the Astronomical Unit value.

The standard parametrisation in terms of the microlensing parallax vector components takes into account the East and North components, i.e. $\pi_{\rm EE}$ and $\pi_{\rm EN}$ respectively, whose composition gives the $\pi_{\rm E}$ vector absolute values

$$\pi_{\rm E} = \sqrt{\pi_{\rm EE}^2 + \pi_{\rm EN}^2} \tag{13}$$

By estimating the values of both the parallax parameter and the Einstein angle, one can combine the equations to obtain a relation for the lens mass (Gould and Salim, 2000)

$$M_L = \frac{\theta_{\rm E}}{\kappa\pi_{\rm E}} \tag{14}$$

where $\kappa \equiv \frac{4G}{c^2\ {\rm AU}} = \frac{3v_\oplus^2}{M_\odot c^2} \simeq 8.144\ \frac{\rm mas}{M_\odot}$ and $v_\oplus \simeq 30$ km s^{-1} is the Earth orbital speed.

Finally, considering Eq. (6), one can also estimate the lens velocity, obtaining in this way some hints on the possible lens nature.

4. Results and discussion

In this paper we presented the discovery of the microlensing event LMC J05074558-65574990 and the results of the performed analysis. Observations show that the source star is quite close to the Earth, being at a distance of about 1.5 kpc.

We model the microlensing event in four different ways: first of all, we consider the simpler Point-Source Point-Lens model, which refers

[5] Since the fit procedure returns the baseline flux in each band, we converted the fluxes into magnitudes by considering the *pyLIMA* zeropoint, i.e. $m_{\rm ZP} = 27.4$, and the relation $m_0 = m_{\rm ZP} - 2.5 \cdot \log_{10} f_s$ (Bachelet et al., 2017).

[6] For the sake of completeness, if the lens-source separation is quite small (i.e. $u \ll 1$), following the Gould approximation (Gould, 1994), the Point-Source amplification in Eq. (4) can be approximated as $A(t) \approx \frac{1}{u}$ and the amplification in the finite-source model can be obtained by solving elliptic integrals (for further details see Witt and Mao 1994, Yoo et al. 2004, Cassan et al. 2006, Lee et al. 2009).

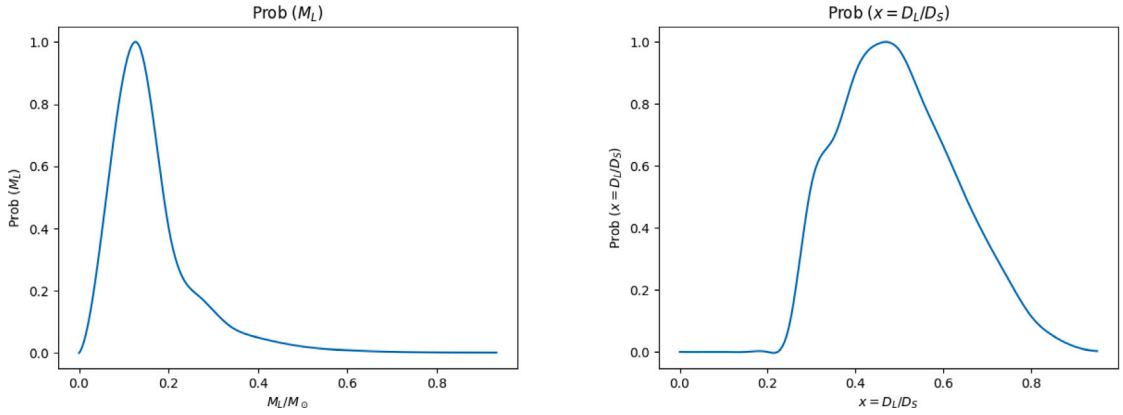

Fig. 4. Probability distributions, obtained from the Monte Carlo procedure described in Ingrosso et al. (2006), for the lens mass M_L in units of solar mass (left panel) and the dimensionless lens distance x (right panel) considering simulated events that satisfy the observational parameters.

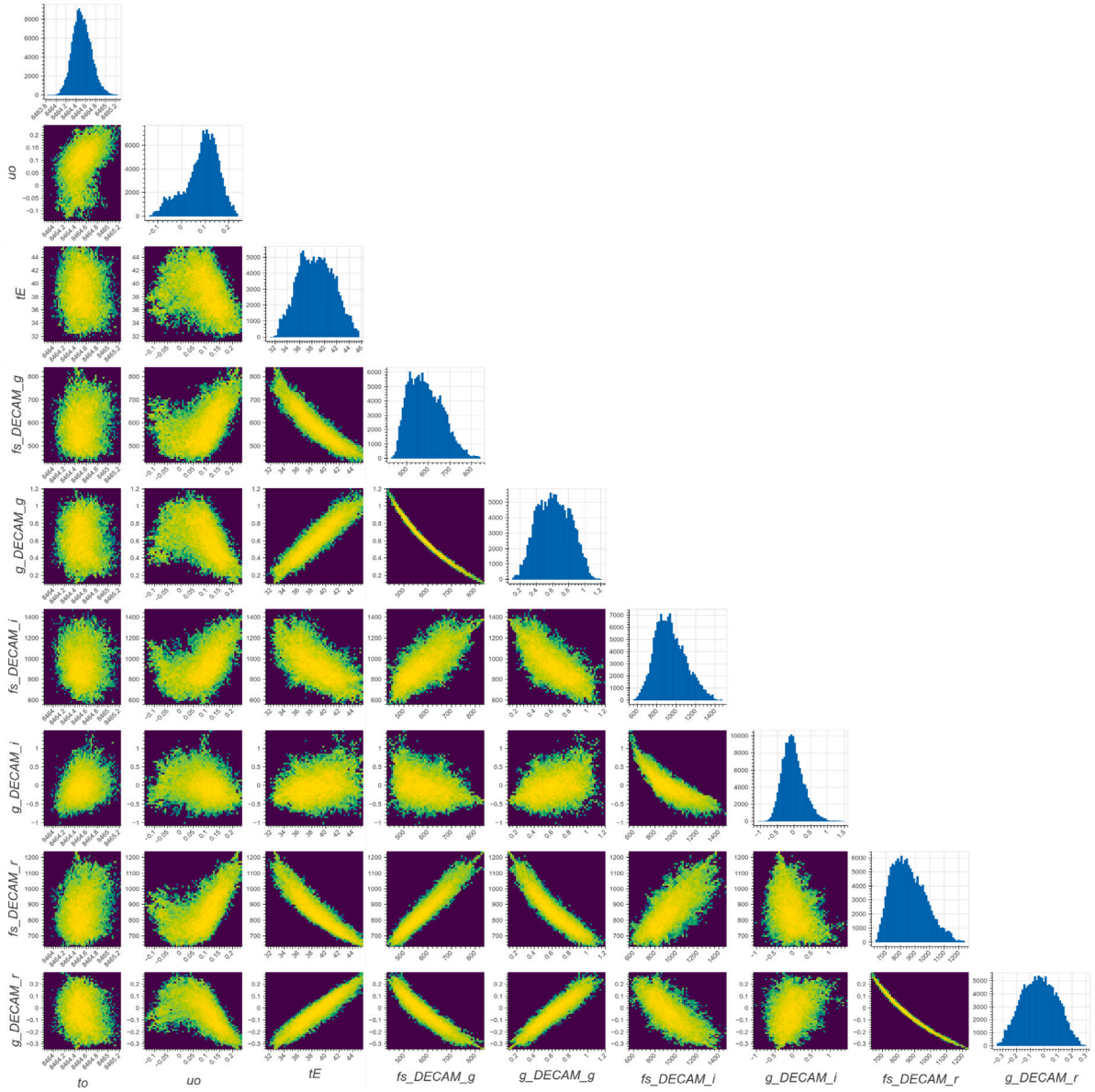

Fig. 5. Corner plot for the PSPL model.

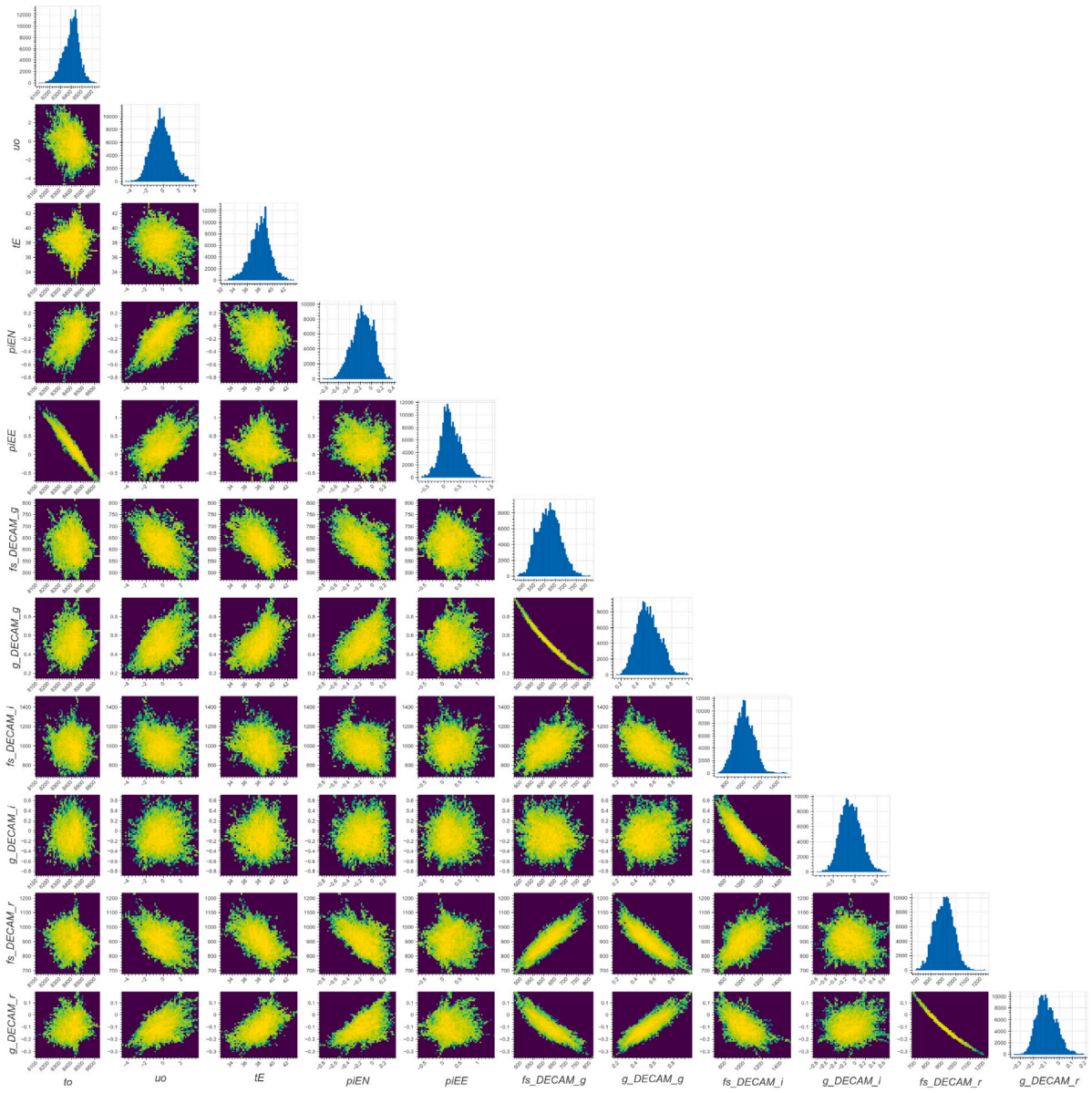

Fig. 6. Corner plot for the PSPL + Earth Parallax model.

to a simple Paczyński light curve. After that, we separately add the parallax and the finite source effect (FSPL) and, at the end, we consider the Finite-Source Point-Lens model taking also into account the Earth parallax effect. The resulted fits for each adopted model mentioned previously are shown in Fig. 2, at the top of each sub-panel: the panels on the top refer to the PSPL (left) and PSPL+Earth Parallax (right) models; the panels on the bottom refer to the FSPL (left) and FSPL+Earth Parallax (right) models. We note that the blue line refers to the best fit of the adopted microlensing model, regarding the observed data in the three bands (g, r and i band). The lower sub-panels report instead the residual between the data and the model. The related best fit parameters are presented in Table 1, associated to the corresponding model taken into account. The error bars shown in Fig. 2 are obtained by multiplying the uncertainties by a constant, defined as the square root of the χ^2/dof value, for each model. The uncertainties are than calculated as

$$\sigma_{\mathrm{mag,i}} = \sigma_{\mathrm{mag,i}} \times \sqrt{\left(\chi^2/dof\right)_{\mathrm{i}}} \tag{15}$$

where i denotes each involved model. Since the $\left(\chi^2/dof\right)_{\mathrm{i}}$ obtained values turn out to be quite similar for the different models, one has $\sqrt{\left(\chi^2/dof\right)_{\mathrm{i}}} \simeq 1.45$. The χ^2/dof values are then scaled to one. In Table 1, the χ^2 and χ^2/dof values, obtained before and after the scaling, are reported for completeness. Moreover, in Figs. 5–8 we present the corner plots with the probability distribution of the parameters involved in the microlensing models. Each column corresponds to a parameter, following the same order as in Table 1 for the corresponding model. The one-dimensional histograms are associated to the estimated Monte Carlo probability distribution of each model parameter, while the other plots show the two-dimensional histograms that correlate each pair of parameters. We would like to point out that we also considered the possibility to fit our data with a binary lens model. Nevertheless, since the data sampling is not very regular and sufficiently dense as one would need to characterise the possible binary systems features, we decided to rely only on the presented models.

We took into consideration all the competitive scenarios in order to account for the light curve of the detected microlensing events. First of all we accounted for the possibility that the Gaia star, lying in the thick-disk of the Milky Way, represents the microlensing lens, while the source is an unresolved star located either in the Galactic halo or in the LMC. With this configuration, considering the lens and

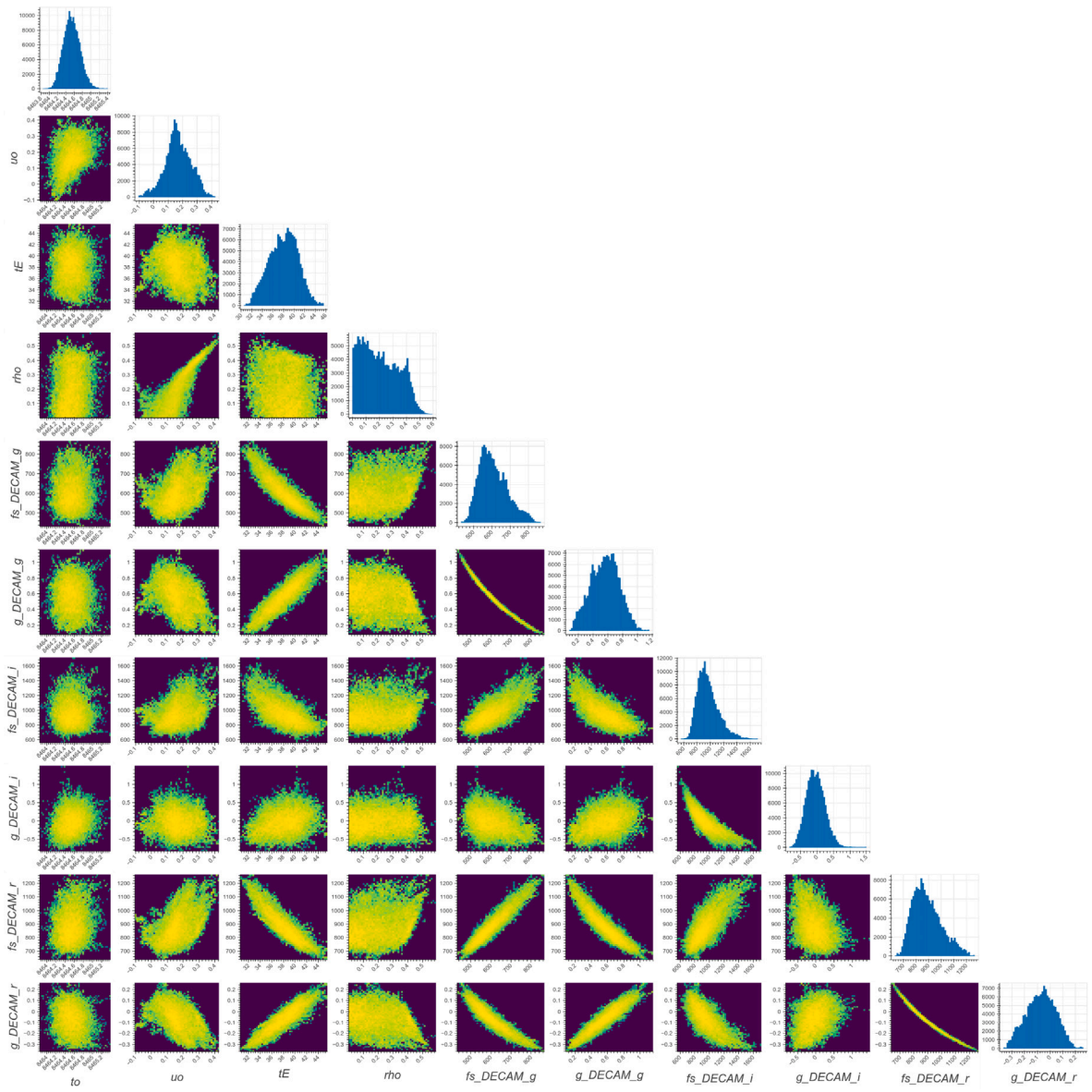

Fig. 7. Corner plot for the FSPL model.

source distances and the lens mass already reported above, estimating the Einstein angle and using Eq. (6) we get a lens crossing velocity $\gtrsim 100$ km/s. Since one would expect a lens speed roughly close to the typical velocities for thick-disk objects, i.e. $\sim 30 \div 50$ km/s, the obtained result seems to be rather weak. Despite the interesting configuration of this scenario, the blending parameter estimated by the microlensing analysis is compatible with zero, thus confirming that the total flux is dominated by the source, the lens nature of the Gaia star seems quite unlikely.

At this point, the most probable configuration considers the Gaia star as the source star of the detected microlensing event, while the lens is some fainter object located between the Earth and the source star. We remind that the candidate lensed source has been catalogued as a star by GaiaDR3 (Gaia Collaboration et al., 2022) and by the Magellanic Clouds Photometric Survey (Zaritsky et al., 2004) located in the Galactic thick-disk at distance $D_S = 1.55^{+0.72}_{-0.53}$ kpc (Bailer-Jones et al., 2021). As introduced in Section 2, the colour-index of the star gives an estimate of the effective temperature, $T_S \simeq 5120$ K, that corresponds to a K1V spectral type object, i.e. a red main sequence star, with a typical radius of $R_S \sim 0.797\ R_\odot$ and mass of $M_S \sim 0.86\ M_\odot$(Pecaut and Mamajek, 2013; Mamajek, 2022).

Considering the microlensing models adopted and the fit results in Table 1, a first look to the χ^2 values might suggest that the FSPL + Earth Parallax model is the best one, even if all other models still show a similar χ^2 values. However, even though more accurate and sophisticated models have been suggested, it appears that the simplest model, i.e. the PSPL model, is the most effective and reliable. Nevertheless, for the sake of discussion, with the assumption that the FSPL + Earth Parallax is chosen as the potential model, the estimate of the lens mass and distance following Eqs. (6) and (14) might suggest a microlensing lens with mass $M_L = 33^{+17}_{-13}\ M_\oplus$ located at $D_L = 1.50^{+0.66}_{-0.49}$ kpc from Earth, suggesting a possible free-floating planet nature for the lens.

With these considerations, we assume the PSPL scenario as the preferred one. This model relies on well-defined and restricted estimates for all the involved parameters. Furthermore, the u_0 values has a more bounded estimate for the first and third models in Table 1: in fact, since the microlensing amplification is related to u_0 as shown in Eq. (4), in the FSPL + Earth Parallax model the amplification should be of the order of 10^2, which involves in the light curve $\Delta m \simeq 5 \div 6$, far from the observed value. In all other cases, the u_0 estimates lead to a $\Delta m \simeq 2 - 3$, which is instead in line with what is observed in the light curves. With reference to the fit parameters, reported in Table 1, we can estimate

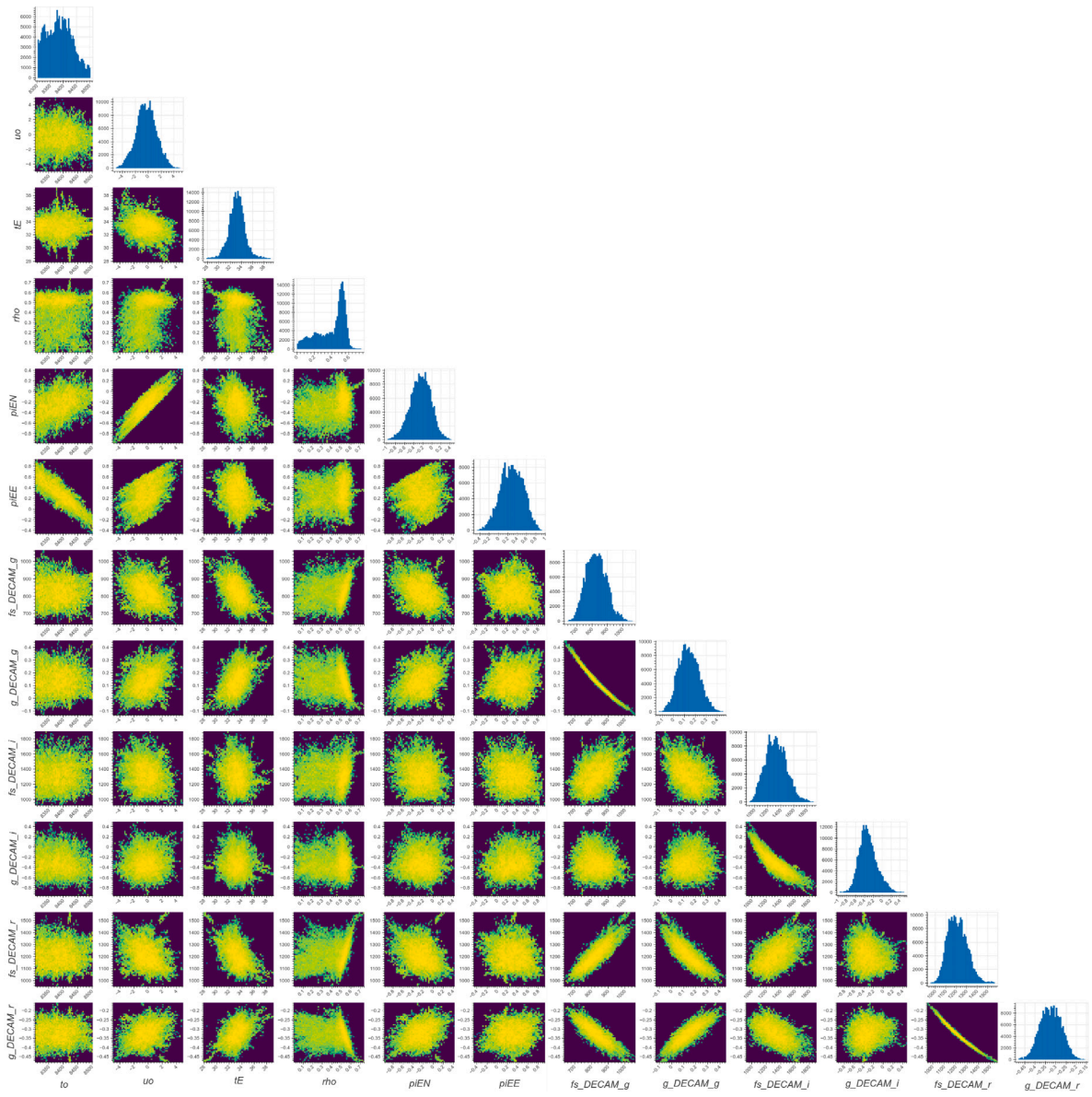

Fig. 8. Corner plot for the FSPL + Earth Parallax model.

the most probable lens distance D_L and mass M_L by using a Monte Carlo procedure (Yee et al., 2012). We modelled the Milky Way with a triaxial bulge (Dwek et al., 1995) and a double exponential stellar disk (Bahcall et al., 1983; Gilmore et al., 1989) and consequently we evaluated the expected microlensing event rate $\Gamma(D_L, D_S, M_L, v_t, \mathscr{M})$ as described in Ingrosso et al. (2006), where $\mathscr{M}$ represents the source absolute magnitude. After defining $x = D_L/D_S$ as the dimensionless lens distance and evaluating the differential rates $d\Gamma/dx$ and $d\Gamma/dM_L$ by integrating over all the remaining relevant quantities, the most likely values of the lens distance and mass can be evaluated as

$$\overline{x} = \int x \left(\frac{d\Gamma}{dx}\right) dx \tag{16}$$

$$\overline{M}_L = \int M_L \left(\frac{d\Gamma}{dM_L}\right) dM_L \tag{17}$$

In this way we obtained an estimate of the average dimensionless lens distance $\overline{x} = 0.50 \pm 0.13$ and average lens mass $\overline{M}_L = (0.16 \pm 0.10) M_\odot$ (see panels in Fig. 4). By converting the $\overline{x}$ value in physical units we obtain the lens distance $D_L = 7.8^{+4.1}_{-3.4} \times 10^2$ pc. In this context, the detected lens can be consider as one of the closest ever detected.

We also pointed out the possibility of estimating the lens mass by photometric considerations. In the PSPL scenario, by considering the results returned by the fit, one obtains that the g-band and r-band magnitudes for the lens are $g_L \gtrsim 21.9$ and $r_L \gtrsim 20.1$ due to the blending factors. By converting the magnitudes from Sloan to the V-Johnson, following Jordi et al. (2006), we obtain $V_L \gtrsim 21$. Considering that the lens distance is surely smaller then the source distance, i.e. $D_L < D_S \simeq 1.55$ kpc, from the definition of the distance modulus we can extract the lower limit of the absolute V magnitude, that comes out to be $V_L^{abs} \gtrsim 10$. From Mamajek (2022), we determine the maximum lens mass, for a main-sequence star, i.e. $M_L \lesssim 0.25 M_\odot$, which agrees with the values obtained from the Monte Carlo.

On the other and, we can also provide an estimate for the lens distance by assuming the lens mass provided by the Monte Carlo, i.e. $M_L \lesssim 0.26 M_\odot$. By considering the previous estimate of the V magnitude $V_L \gtrsim 21$, and assuming an absolute magnitude $M_V \gtrsim 12.5$ (as reported in Mamajek 2022), from the distance modulus we can estimate a lens distance $D_L \gtrsim 500$ pc that, even is this case, agrees with the Monte Carlo estimate.

The event presented here may also provide further motivation for the study of dark matter and primordial objects possibly formed in

the initial stage of the universe and nowadays distributed in the thick Galactic disk. Past, current and, particularly, future surveys, including OGLE (Udalski et al., 1993), Gaia (Gaia Collaboration et al., 2016), and the Vera Rubin Observatory (Ivezić et al., 2019), are crucial in mapping the Galaxy looking for hidden dark microlensing objects, as well as for the study of stellar populations in the thick Galactic disk, whose recent investigation shows evidence of an older stellar population (see, e.g., Carollo et al. 2019).

CRediT authorship contribution statement

A. Franco: Conception and design of study, Acquisition of data, Analysis and/or interpretation of data, Writing – original draft, Writing – review & editing. **A.A. Nucita:** Conception and design of study, Acquisition of data, Analysis and/or interpretation of data, Writing – original draft, Writing – review & editing. **F. De Paolis:** Conception and design of study, Acquisition of data, Analysis and/or interpretation of data, Writing – original draft, Writing – review & editing. **F. Strafella:** Conception and design of study, Acquisition of data, Analysis and/or interpretation of data, Writing – original draft, Writing – review & editing.

Declaration of competing interest

The authors declare that they have no known competing financial interests or personal relationships that could have appeared to influence the work reported in this paper.

Data availability

Data will be made available on request.

Acknowledgements

This paper is based on publicly available observations by DECam (Dark Energy Camera), an instrument mounted on the V. Blanco Telescope, as part of the Cerro Tololo Inter-American Observatory (Chile). DECam images used for this work are publicly available at the https://astroarchive.noirlab.edu/portal/search/#/search-form webpage.

We warmly thank Prof. Gabriele Ingrosso for useful suggestions and advice and for friendly discussions. We thank the anonymous Referees for useful suggestions. We also thank for partial support the INFN projects TAsP and Euclid.

All authors approved the version of the manuscript to be published.

References

Alard, C., 2000. A & AS 144 (363).
Alard, C., Lupton, R.H., 1998. ApJ 503 (325).
Alcock, C., et al., 1995. ApJL 454 (L125).
Alcock, C., et al., 1996. ApJL 461 (84).
Bachelet, E., et al., 2017. AJ 154 (203).
Bahcall, J.N., et al., 1983. ApJ 265 (730).
Bailer-Jones, C.A.L., et al., 2021. ApJ 161, 147.
Ballesteros, F.J., 2012. EPL 97 (34008).
Carollo, D., et al., 2019. ApJ 887 (22).
Cassan, A., et al., 2006. A & A 460 (277).
De Paolis, F., et al., 2016. Universe 2 (6).
Dwek, E., et al., 1995. ApJ 445 (716).
Einstein, A., 1936. Science 84 (506).
Flaugher, B., et al., 2015. AJ 150 (150).
Franco, A., et al., 2023a. The Sixteenth Marcel Grossmann Meeting http://dx.doi.org/10.1142/13149, https://doi.org/10.1142/13149.
Franco, A., et al., 2023b. New Astronomy 103, 102043.
Gaia Collaboration, Prusti, T., et al., 2016. A & A 595, 36, id.A1.
Gaia Collaboration, Vallenari, A., Brown, A.G.A., et al., 2022. arXiv:2208.00211.
Gilmore, G., et al., 1989. ARA & A 27 (555).
Gould, A., 1992. ApJ 392 (442).
Gould, A., 1994. ApJ 421 (L71).
Gould, A., Salim, S., 2000. Astrophys. J. 524 (794).
Ingrosso, G., et al., 2006. MNRAS 476 (3), 2962.
Irwin, M.J., et al., 1989. Astron. J. 98 (1989).
Ivezić, Ž., et al., 2019. ApJ 873 (2), 111, 44.
Jordi, K., et al., 2006. A & A 460 (1), 339.
Lang, K.R., 1992. Astrophysical Data: Planets and Stars. Springer-Verlag New York, Inc.
Lee, C.-H., et al., 2009. ApJ 695 (200).
Mamajek, E., 2022. A modern mean dwarf stellar color and effective temperature sequence. Version 2022.04.16, http://www.pas.rochester.edu/emamajek/EEM_dwarf_UBVIJHK_colors_Teff.txt.
Paczyński, B., 1986. ApJ 304 (1).
Paczyński, B., 1996. ARA & A 34 (419).
Palanque-Delabrouille, N., et al., 1998. v 332 (1).
Pecaut, M.J., Mamajek, E.E., 2013. ApJS 208 (9).
Schlafly, E.F., Finkbeiner, D.P., 2011. ApJ 737 (2), id. 103.
Stetson, P.B., 1996. Users manual for DAOPHOT II.
Tonry, J.L., et al., 2018. ApJ 867 (105).
Udalski, A., et al., 1993. Acta Astron. 43 (289).
Witt, H.J., Mao, S., 1994. ApJ 430 (505).
Yee, J., et al., 2012. ApJ 755 (102).
Yoo, J., et al., 2004. ApJ 603 (139).
Zaritsky, D., et al., 2004. AJ 128 (1606).